



A study of uplink and downlink channel spatial characteristics in an urban micro scenario at 28 GHz*

Tao JIANG[†], Jianhua ZHANG^{†‡}, Pan TANG, Lei TIAN

*State Key Lab of Networking and Switching Technology,
 Beijing University of Posts and Telecommunications, Beijing 100876, China*

[†]E-mail: jet@bupt.edu.cn; jhzhang@bupt.edu.cn

Received Aug. 31, 2020; Revision accepted Jan. 6, 2021; Crosschecked Feb. 4, 2021; Published online Mar. 29, 2021

Abstract: This paper presents an empirical study of the uplink and downlink azimuth angle of arrival (AoA) in an urban micro (UMi) scenario at 28 GHz. At present, most UMi measurements are conducted in the downlink and then the uplink situation is inferred assuming channel reciprocity. Although the channel correlation coefficient of the uplink and downlink can be as high as 0.8, this does not mean that they are the same. Only a real uplink measurement can accurately describe its channel conditions, and this is what this study does. A receiver equipped with a rotatable horn antenna is mounted at the base station and the user terminal, respectively, in simulating the uplink and downlink. To improve the angular resolution, we extract the multipath components (MPCs) using the space-alternating generalized expectation-maximization algorithm. Also, a spatial lobe approach is used to cluster the MPCs in the power angular spectrum. By matching MPCs with objects in the environment, we find that direct propagation and first-order reflections are dominant in line-of-sight and non-line-of-sight cases. By comparing our measurement with those in standard channel models, we verify that the AoA of clusters follows a Gaussian distribution in the uplink and downlink. In addition, a two-dimensional Gaussian distribution for ray AoA and power is established to reflect their correlation.

Key words: Channel measurements; Millimeter-wave (mmWave); Uplink; Downlink; Azimuth angle of arrival
<https://doi.org/10.1631/FITEE.2000443> **CLC number:** TN928

1 Introduction

Today, the fifth-generation (5G) cellular radio system has been widely used around the world and satisfies the explosive demand for mobile data services. However, restricted to the base station (BS) coverage and the cost of mobile network evolution, the currently used 5G frequency bands are concentrated mainly at the C-band (3.3–4.2 GHz and

4.4–5 GHz). Moreover, the continuous spectrum of mobile business is ≤ 200 MHz to avoid conflicts with other communication businesses. To overcome the shortage of spectrum resources, millimeter-wave (mmWave) bands are considered as a promising technology for the future (You et al., 2020). At the World Radiocommunication Conference 2019 (WRC-19), the frequency bands 24.25–27.5, 37–43.5, 45.5–47, 47.2–48.2, and 66–71 GHz were newly identified as additional radio-frequency bands for international mobile telecommunications (IMT) worldwide. The European Commission has begun to harmonize the 24.25–27.5 GHz band for 5G systems in May 2019, and update the relevant technical conditions applicable to this band in April 2020. The State Radio Regulation of China also plans to amend the application

[‡] Corresponding author

* Project supported by the Outstanding Youth Fund of National Natural Science Foundation of China (No. 61925102), the National Key R&D Program of China (No. 2020YFB1805002), the National Natural Science Foundation of China (No. 62031019), and the BUPT-CMCC Joint Innovation Center

ORCID: Tao JIANG, <https://orcid.org/0000-0001-5369-8068>; Jianhua ZHANG, <https://orcid.org/0000-0002-6492-3846>

© Zhejiang University Press 2021

regulations for 5G mmWave bands in coming years.

As a fundamental part of the mobile communication system, the mmWave wireless propagation channel determines the optimum performance of systems (Shafi et al., 2018; Zhang JH et al., 2020). Through the real field measurements, researchers can effectively model the spatial-time-frequency characteristics of the wireless channel. Due to the significant propagation loss of mmWave (Zhang JH et al., 2017), the horn antenna is widely used for power compensation in outdoor measurements. In Rappaport et al. (2013), an urban measurement was conducted with horn antennas at 37.625 GHz to study the angle of arrival (AoA), delay spread, and propagation loss. A measurement with bands of 500 MHz was conducted at 28 and 38 GHz in Park et al. (2016). Its multipath components (MPCs) in directional channel impulse responses (CIRs) were extracted using the space-alternating generalized expectation-maximization (SAGE) algorithm. The delay spread and AoA in clusters were then compared in line-of-sight (LoS) and non-line-of-sight (NLoS) cases. In Zhao et al. (2019), a virtual single-input multiple-output (SIMO) measurement system was set up using a horn antenna. Based on the collected data, a neural network channel-modeling and a simulation framework were proposed.

However, the above studies still have two places that need to be improved:

The first is that most mmWave channel measurements simulate only a downlink condition by setting transmitter (TX) on the rooftop and receiver (RX) on the ground. Although the uplink channel can be generated by swapping the arrival and departure parameters of the downlink (3GPP, 2019), the parameters are not the same. In frequency division duplex (FDD) measurements, the correlation coefficient of uplink power angular spectrum (PAS) and downlink PAS is 0.84, and the correlation coefficient of angular spread (AS) is 0.83 (Pedersen et al., 1999). A rich multipath environment may weaken the channel reciprocity (Foo et al., 2002). As for time division duplex (TDD) measurements, the channel situation will be disturbed by people's movement, vehicular traffic (Bigler et al., 1995), and antenna height (Alatossava et al., 2007). When the measurement case changes from LoS to NLoS, the correlation coefficient of the uplink and downlink channels decreases by 0.02 in He et al. (2009) and decreases by

0.12 in Hamida et al. (2010).

The second is that the cluster results of the KPower-Means algorithm cannot remain consistent with random initialization procedures (Samimi and Rappaport, 2016b). In addition, the KPower-Means algorithm considers different parameters, such as the delay, power, and angle, at the same time. Because these parameters have different physical meanings, their assigned weights should be different when calculating the maximum close distance (MCD).

To supplement the knowledge of uplink channels, we design an uplink experiment in this study. As shown in Fig. 1a, an omnidirectional antenna is placed at the user terminal (UT) side to act as a TX, and a rotatable horn antenna is placed at the BS side to receive the signal. The downlink measurements are conducted at the same positions. As shown in Fig. 1b, a sector antenna is placed at the BS side to simulate the TX, and a rotatable horn antenna is placed at the UT side to act as the RX. To overcome the shortcomings of the KPower-Means algorithm, we use the time cluster-spatial lobe (TCSL) method to cluster MPCs in a lobe shape in the spatial domain. This approach was proposed in Samimi and Rappaport (2016a, 2016b), and decouples the time and space dimensions by extracting temporal and spatial statistics separately. The TCSL method is originally used to cluster the scanning PAS, which may reduce the spatial resolution of MPCs (Jiang et al., 2017). In this case, we extract MPCs by the

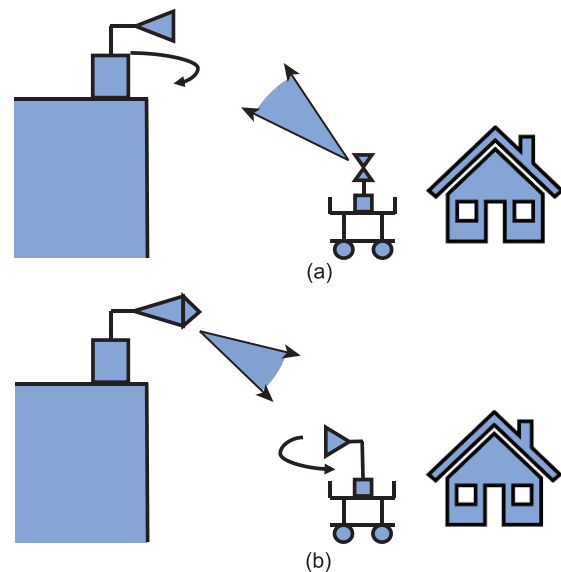


Fig. 1 Illustration of the uplink (a) and downlink (b) in this study

SAGE algorithm and then cluster them in a lobe shape in the spatial domain. Using this method, the angular resolution of MPCs changes from 5° to 1.25° , and the intra-cluster angular characteristics can be modeled. Based on the cluster results, we have the following findings:

1. The relationship between the cluster width and power is modeled by an exponential function.
2. The AoA distribution of the cluster is more in line with the Gaussian distribution.
3. A two-dimensional Gaussian distribution is proposed to describe ray AoA and power.

2 Measurement campaign

2.1 Measurement environment

This series of measurements was conducted in a typical UMi environment at Beijing University of Posts and Telecommunications (BUPT). The environment layout is as shown in Fig. 2. The BS antenna is on the top of Science Hall (building 1) with a height of 12.4 m above the ground. UTs are placed at 10 different positions, and their antenna height is 1.8 m above the ground. The two-dimensional distance between the BS and the UT is between 25.5 m (position 1) and 164 m (position 8). All UT positions are divided into LoS and NLoS cases. Among them, positions 1, 3, 4, 5, 6, 7, and 8 are in the LoS case. Positions 2, 9, and 10 are in the NLoS case because

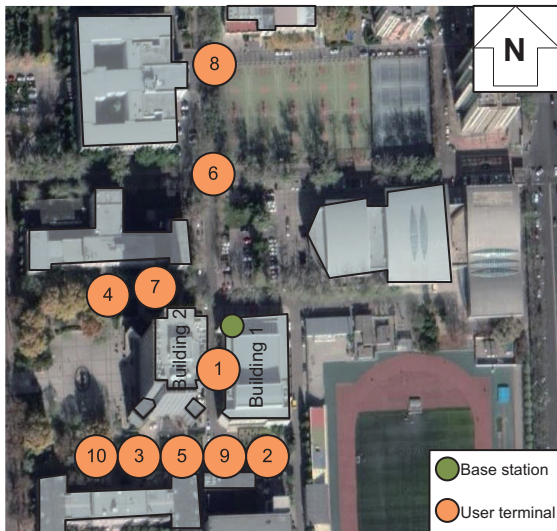


Fig. 2 Top view of the measurement environment from the Baidu map

of the obstructions from buildings 1 and 2.

2.2 Measurement system

Measurements are performed by a broadband realtime spread-spectrum channel sounder (Jiang et al., 2020). A pseudo-noise (PN) sequence with a code length of 511 is generated at a 400-Mbaud symbol rate on the TX side. The output power reaches 24 dBm with the help of a power amplifier. On the RX side, the sampling rate of I/Q data is 1.2 GS/s, and the minimum detectable signal level is -107 dBm when equipping a low-noise amplifier.

We use the “directional antenna scanning” method to obtain the arrival angle information in the uplink and downlink. The antenna parameters are illustrated in Table 1. The uplink is as shown in Fig. 1a. A biconical antenna is used at UT to transmit the signal, and a horn antenna is mounted on a rotator on the BS side to receive signals. Because the horn antenna height is only 30 cm above the roof wall, the alternative angle of depression is limited from 0° to -20° . During the measurement, the horn antenna points to three elevation angles: 0° , -10° , and -20° . The horizontal scanning range is from 0° to 360° , and its rotation step is 5° .

Table 1 Antenna parameters (Tang et al., 2018)

Type	$\phi_{3dB} (^\circ)$	$\theta_{3dB} (^\circ)$	Gain (dBi)
Horn	11	10	25
Biconical	360	40	3
Sector	92.19	40.15	9

The downlink condition is as shown in Fig. 1b. To simulate the real transmission situation at the BS, we use a sector antenna to enhance the coverage. During the measurement, its direction always points to the UT. A rotatable horn antenna is located on the UT side. Its horizontal scanning range is from 0° to 360° with a rotation step of 5° . The elevation angle of the horn antenna is set differently to receive the strongest signal:

1. The elevation angle points at 0° , 10° , and 20° when the UT is at positions 2, 3, 4, 5, 6, 7, 8, 9, and 10.
2. The elevation angle points at 40° , 50° , and 60° when the UT is at position 1.

3 Power angular spectrum of the arrival angle

The azimuth power angular spectrum reflects the power distribution on the angular domain. This characteristic is affected by the reflector positions. Its distribution is defined to follow the wrapped Gaussian distribution in channel standards.

Before measuring the uplink and downlink, we calibrate the system and obtain CIRs at each pointing angle as (Gao et al., 2016)

$$h_{i,j,k}(\tau) = \sum_{l_{i,j,k}=1}^{L_{i,j,k}} \alpha_{l_{i,j,k}} \sigma(\tau - \tau_{l_{i,j,k}}), \quad (1)$$

where i, j, k are the indices of the azimuth angle, elevation angle, and measurement position, respectively. Their maximum values are 72, 3, and 10, respectively. $l_{i,j,k}$ is the path index, and its maximum is $L_{i,j,k}$. $\alpha_{l_{i,j,k}}$ is the complex magnitude and $\tau_{l_{i,j,k}}$ is the delay. To have the scanning PAS of each measurement position, the CIR of each pointing angle is summed as

$$\text{PAS}_{i,j,k} = \int \|h_{i,j,k}(\tau)\|^2 d\tau. \quad (2)$$

The horn antenna rotation measurement can also be viewed as a SIMO measurement. CIRs that result from different pointing angles are synchronized using the same clock (Zhan et al., 2018; Zhang PZ et al., 2018; Lv et al., 2019). In this way, the SAGE algorithm can be used to estimate the delay and angular information (Fleury et al., 1999), and the spatial resolution increases from 5° to 1.25° . The expression of the spatial-temporal CIR can be rewritten as

$$h_k(\phi, \theta, \tau) = \sum_{l_k=1}^{L_k} \alpha_{l_k} \sigma(\phi - \phi_{l_k}) \sigma(\theta - \theta_{l_k}) \sigma(\tau - \tau_{l_k}), \quad (3)$$

where ϕ and θ are the estimated azimuth and elevation angle, respectively. Only three elevation angles are scanned on the UT/BS side, which is not sufficient to obtain all elevation information. We just focus on the azimuth angles in the following. The SAGE PAS at the k^{th} measurement position is expressed as

$$\text{PAS}_k(\phi) = \iint \|h_k(\phi, \theta, \tau)\|^2 d\theta d\tau. \quad (4)$$

We plot the uplink and downlink PAS of positions 1, 2, 4, and 10 in Fig. 3. Note that scanning

PASs and SAGE PASs belong to two different categories. For the scanning PASs, we select the minimum value among all received uplink and downlink powers as the divisor, and then use the power of different angles to divide this minimum value. Its calculation is shown in Eq. (5). The SAGE PASs are calculated in a similar manner, as shown in Eq. (6). However, because the antenna pattern has been eliminated in the SAGE PASs, its minimum power is lower than that of the scanning PASs, which causes the SAGE PASs to have a larger dynamic range in Fig. 3.

$$\text{PAS}_{\text{scan}_{i,j,k}} = 10 \lg \left(\frac{\text{PAS}_{i,j,k}}{\min(\text{PAS}_{i,j,k})} \right), \quad (5)$$

$$\text{PAS}_{\text{sage}_k}(\phi) = 10 \lg \left(\frac{\text{PAS}_k(\phi)}{\min(\text{PAS}_k(\phi))} \right). \quad (6)$$

From Fig. 3 we can see that the power difference between the uplink and downlink is between 2 dB and 9 dB in scanning PASs and between 6 dB and 20 dB in SAGE PASs. The minimum power is different in scanning PASs and SAGE PASs; one reason is that different TX antenna types are used in the uplink and downlink. The sector antenna gain is 6 dBi greater than the biconical antenna gain, which makes the power difference ≥ 6 dB in SAGE PASs.

By matching SAGE PASs with the environment, we can infer the dominant propagation directions of clusters in Fig. 4. It can be seen that the clusters in LoS cases contain mainly direct paths and first-order reflections. We summarize the percentage of the power of the direct path and first-order reflections in LoS cases in Table 2. From this table, we

Table 2 Percentage of power of the direct path and first-order reflections in LoS cases

Position	Percentage of power			
	Uplink		Downlink	
	Dir	FR	Dir	FR
1	97.05%	2.95%	90.08%	9.91%
3	99.61%	0.39%	82.83%	15.77%
4	100.00%	0.00%	93.75%	6.25%
5	86.44%	13.56%	96.32%	3.68%
6	99.44%	0.56%	97.08%	2.92%
7	100.00%	0.00%	92.57%	6.66%
8	100.00%	0.00%	99.64%	0.36%

Dir represents the direct path; FR represents the first-order reflections

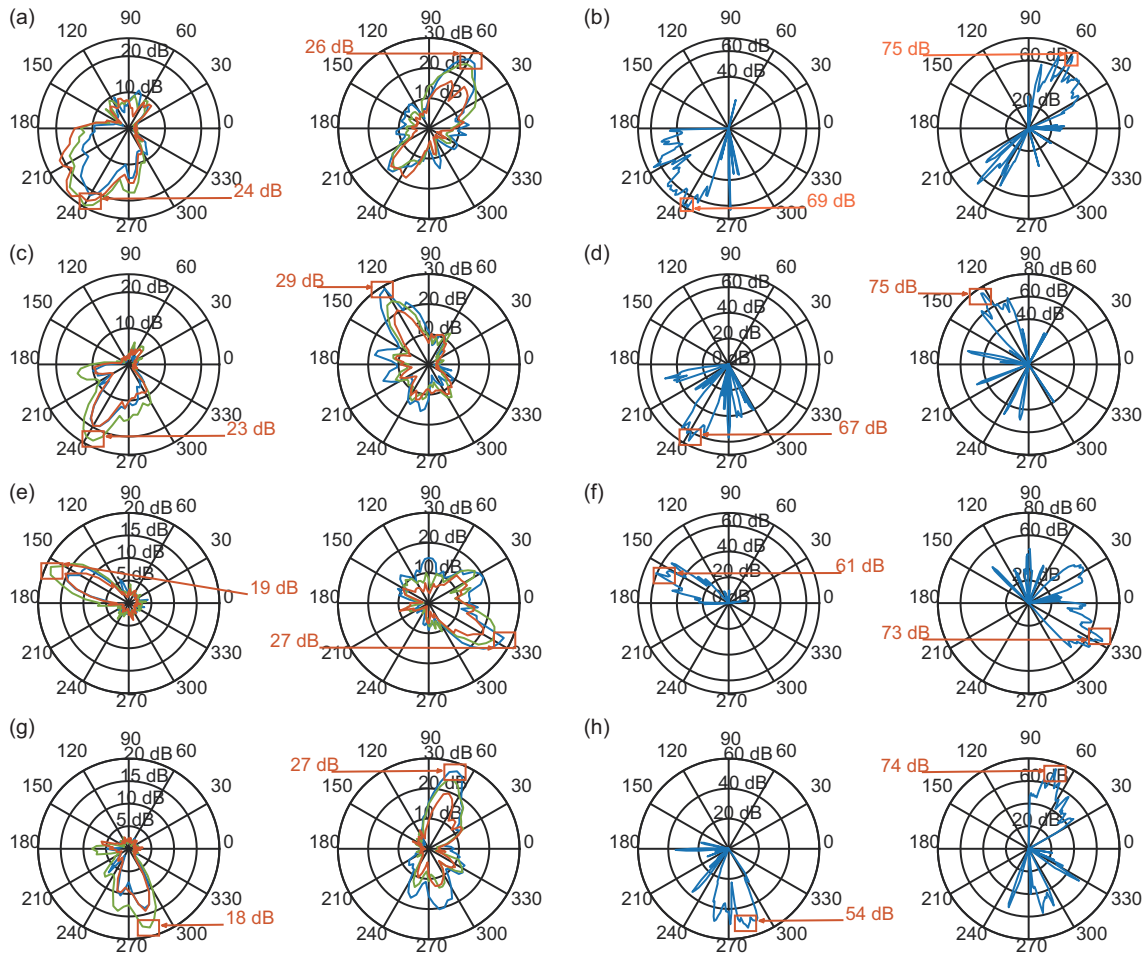


Fig. 3 Power angular spectrum (PAS) at four typical positions. In the sub-figures, the left one is the uplink condition, and the right one is the downlink condition. (a) Scanning PAS at position 1 (LoS); (b) PAS of SAGE at position 1 (LoS); (c) Scanning PAS at position 2 (NLoS); (d) PAS of SAGE at position 2 (NLoS); (e) Scanning PAS at position 4 (LoS); (f) PAS of SAGE at position 4 (LoS); (g) Scanning PAS at position 10 (NLoS); (h) PAS of SAGE at position 10 (NLoS)

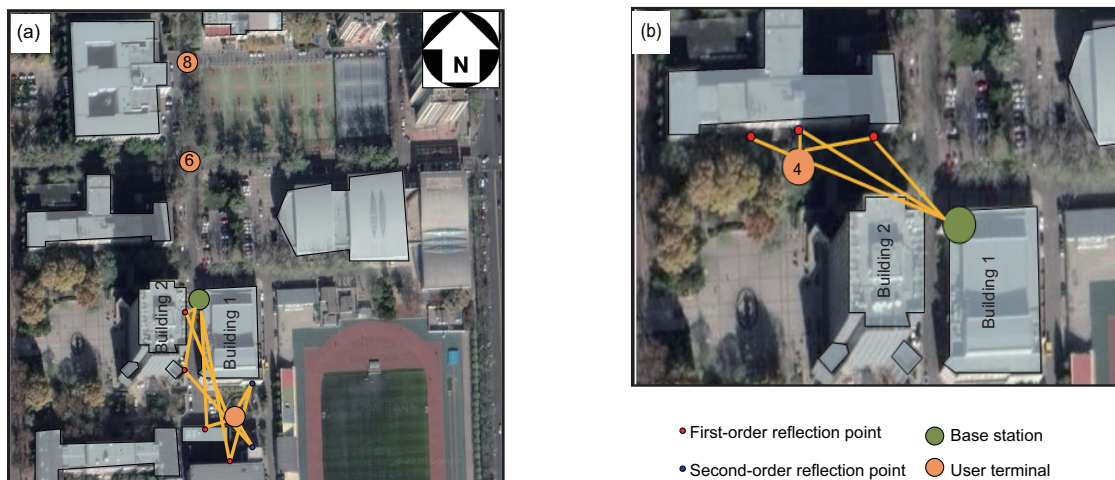


Fig. 4 Multipath components (MPCs) matching between the power angular spectrum and the environment: (a) MPCs of position 2 (NLoS); (b) MPCs of position 4 (LoS)

can see that the power percentage of the direct path is between 86.44% and 100%, and the remnant power is caused mainly by first-order reflections. The received MPCs at the BS side are concentrated within 90°, and there is no wave coming from the back of the antenna. This observation is consistent with the results in Rappaport et al. (2013). The dispersion of the downlink AoA in LoS and NLoS cases is similar. However, the distribution of the uplink AoA is more diffuse in NLoS cases. The range of the AoA increases to 120°. The first- and second-order reflections reign in all propagation types in NLoS cases, but the power of second-order reflections is very limited, and is only 0.13% of the total received power at position 2.

4 Azimuth angle spread of arrival

The angular spread can adequately reflect the fluctuation of angles. When modeling the channel angular information, we need to know the distribution of the PAS, but the standard deviation of the distribution is also important. The angular spread and standard deviation are similarly significant and the angular spread can be derived from the standard deviation.

Generally, angular spread calculation involves the minimum second-order central moments of the circular-shift PAS. Here we adopt the method in 3GPP (2019) to calculate the ASA at the k^{th} position:

$$\phi_{\text{ASA}_k} = \sqrt{-2\ln\left(\left|\frac{\int \exp(j\phi)\text{PAS}_k(\phi)d\phi}{\int \text{PAS}_k(\phi)d\phi}\right|\right)}. \quad (7)$$

The power weighted mean AoA is given by

$$\mu_{\phi_k} = \arg\left\{\int \exp(j\phi)\text{PAS}_k(\phi)d\phi\right\}. \quad (8)$$

The LoS and NLoS ASA results are plotted in Fig. 5. We can see that the ASA is larger in downlink conditions for most measurement positions (positions 1, 3, 4, 6, 7, 8, 9, and 10). Only positions 2 and 5 have a larger ASA in uplink conditions. We use $\phi_{\text{ASA,diff}}$ to represent the ASA difference between the uplink and downlink. As shown in Table 3, the positive $\phi_{\text{ASA,diff}} \leq 6^\circ$, but the negative values are between -0.8° and -42.1° . After taking the average of all $\phi_{\text{ASA,diff}}$, we obtain the mean ASA values of the uplink and downlink as 13.3° and 28.8° , respectively. Their ASA difference is -15.6° . We also compare our results with those of the 3GPP TR 38.901 model and mmMAGIC model in Table 4 (Peter et al., 2017). Although the 3GPP TR 38.901 model is applicable for mmWave, its ASA results are all larger than our measurement results except for the uplink in NLoS cases. A more significant ASA difference between the LoS and NLoS cases is observed in our

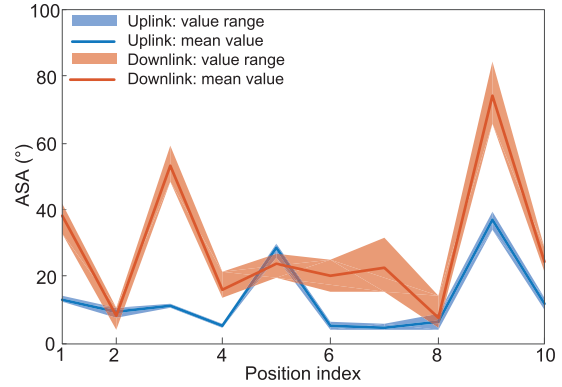


Fig. 5 Angular spread at LoS and NLoS positions

Table 3 Parameters of the uplink and downlink

Position	$\phi_{\text{ASA}}(^{\circ})$			$\mu_{\phi} (^{\circ})$		Number of clusters		c_{ASA}	
	Uplink	Downlink	$\phi_{\text{ASA,diff}}$	Uplink	Downlink	Uplink	Downlink	Uplink	Downlink
1 (LoS)	13.1	38.5	-25.4	233.5	59.8	3	6	4.1	2.4
2 (NLoS)	9.4	8.2	1.2	242.1	123.2	6	7	2.3	1.2
3 (LoS)	11.2	53.3	-42.1	268.4	78.1	5	7	2.8	6.2
4 (LoS)	5.1	15.9	-10.9	154.8	334.8	4	7	1.8	2.5
5 (LoS)	28.7	23.6	5.1	262.4	89.4	4	4	3.9	3.6
6 (LoS)	5.2	20.3	-15.0	96.4	273.4	4	7	1.5	3.1
7 (LoS)	4.5	22.8	-18.3	145.9	327.2	3	10	2.3	2.8
8 (LoS)	6.6	7.4	-0.8	94.6	269.3	2	7	2.4	1.5
9 (NLoS)	37.1	74.2	-37.0	217.4	121.8	4	4	4.6	8.7
10 (NLoS)	11.7	24.2	-12.5	280.4	68.9	5	5	3.2	2.3

Table 4 Comparison with standard models (3GPP, 2019; Samimi and Rappaport, 2016a; Peter et al., 2017)

Case	$\phi_{ASA}(^{\circ})$				Number of clusters				c_{ASA}			
	Uplink		Downlink		Uplink		Downlink		Uplink		Downlink	
	LoS	NLoS	LoS	NLoS	LoS	NLoS	LoS	NLoS	LoS	NLoS	LoS	NLoS
TR 38.901	13.7	15.6	41	49.3	12.0	19.0	12.0	19.0	3.0	10.0	17.0	22.0
mmMAGIC	28.6	7.6	25.5	27.5	2.0	3.0	2.0	3.0	3.0	10.0	15.0	22.1
TCSL	—	—	—	—	1.9	1.6	1.8	1.6	8.5	9.0	10.5	10.1
Our measurement	10.4	19.2	26.3	37	3.5	5	6.9	5.3	2.7	3.3	3.1	4.1

“—” means the value is not defined in the model. According to the channel reciprocity, the 3GPP TR 38.901 and mmMAGIC models consider the α_{ASA} and c_{ASA} in the uplink as equal to the α_{ASD} and c_{ASD} in the downlink, respectively, and the cluster numbers are the same in the uplink and downlink

measurement, which means that the reflections play a more critical role in mmWave channels. The ASA values for the mmMAGIC model vary slightly except for the uplink in NLoS cases (only 7.6°), and no natural conclusions can be drawn from the mmMAGIC model.

The power-weighted mean AoAs are plotted in Fig. 6. It can be seen that the mean AoAs of the uplink and downlink are symmetrical. For easier expression in polar diagrams, we assume the line connecting 180° and 0° is the x axis, the line connecting 270° and 90° is the y axis, and the point with zero radii is the original point. From Fig. 6a we can see that the power-weighted mean AoA of the uplink and downlink are symmetrical around the original point in LoS cases, which means that the direct path is the dominant part in received signals. As for the NLoS cases in Fig. 6b, the mean AoAs are symmetrical around the x axis, which is caused by the first-order reflection. As shown in Fig. 2, buildings 1 and 2 are parallel with the y axis, and provide the main reflecting power. If higher-order (higher than first-order)

reflections carry the dominant power in the scene, power-weighted AoAs will not distribute symmetrically around the x axis.

5 Cluster of azimuth angle of arrival

5.1 Number of clusters

During signal propagation, MPCs that are caused by the same reflector or propagate in the same LoS direction arrive in cluster form. The paths belonging to the same cluster have similar large- and small-scale characteristics. To simplify channel modeling complexity, the standard models always use the clusters as the minimum modeling unit. Then we can construct a complete wireless channel by summing all clusters. Before modeling the channel, we first need to classify the clusters as accurately as possible.

To avoid the misconvergence of the KPower-Means algorithm due to a random initialization procedure, we use the TCSL method to cluster MPCs in the spatial domain (Samimi and Rappaport, 2016a, 2016b). The spatial lobe (SL) here denotes a strong direction of arrival (or departure) where energy is received contiguously in the azimuth and/or elevation dimensions.

The TCSL method is originally used for the scanning PAS. The spatial information of the channel is modeled in a lobe shape (Fig. 7). Each lobe is constructed using the angles whose power is larger than the threshold. According to Samimi and Rappaport (2016a), the power threshold is set to -10 dB, which relates to the maximum received angle power. From Fig. 7 we can see that there are two lobes in the uplink and three lobes in the downlink. Some effective lobes below -10 dB are aborted. Although we can lower the threshold to obtain these lobes, we

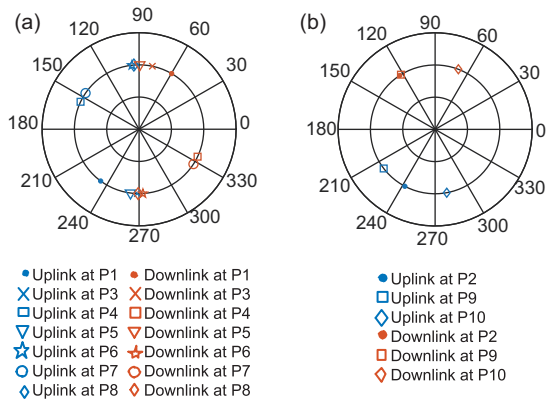


Fig. 6 Distribution of power-weighted mean angles in azimuth: (a) mean azimuth angles of LoS positions; (b) mean azimuth angles of NLoS positions

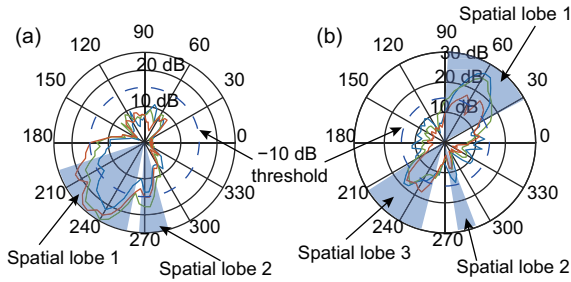


Fig. 7 Identification of lobes at position 1: (a) uplink; (b) downlink

cannot tell whether they are real MPCs or are just caused by the horn antenna pattern.

To solve this problem, we apply the TCSL method to the SAGE PASSs, which have already removed the horn antenna effect. The $PAS_{sage_k}(\phi)$ is split into lobe-shaped clusters when the AoA interval of MPCs is larger than the rotation step (5° in our measurement). The orange sectors in Fig. 8 represent the lobe-shaped clusters. The numbers of clusters in the uplink and downlink are shown in Table 3. The average numbers of clusters are 4 and 6 in the uplink and downlink, respectively. In the LoS cases, the number difference of clusters between the uplink and downlink is 3.3. In the NLoS cases, the maximum number difference is only 1. Because the reflection channels constructed by the surrounding buildings are similar to a spatial filter, the signals in NLoS cases have less freedom in the propagation direction. Although there are many reflective objects around the UT, most of them will form high-order reflections in NLoS cases. Because we know that high-order reflections decay quickly in mmWave bands, the remnant power comes mainly from the first-order reflections after passing this spatial filter. Therefore, the cluster numbers of uplinks and downlinks are similar in NLoS cases.

We also compare our measurement with the standard models in Table 4. The results show

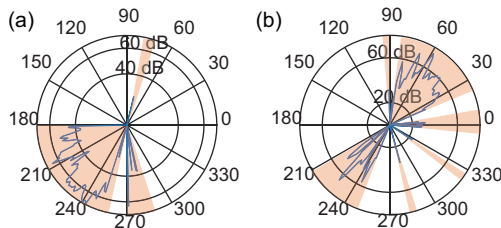


Fig. 8 Cluster results of AoA at position 1: (a) uplink; (b) downlink

References to color refer to the online version of this figure

that the number of clusters obviously decreases in mmWave bands. Because the 3GPP TR 38.901 model is derived from the data sets between 0.5 GHz and 100 GHz, it has the largest number of clusters in the UMi scenario—12 in LoS and 19 in NLoS cases. The mmMAGIC model focuses on the bands from 6 to 100 GHz and has 2–3 clusters. The TCSL model is based on the measurements at 28 GHz and 73 GHz and has the smallest mean number of lobes, distributed from 1.6 to 1.9. The number of lobe-shaped clusters in our measurement is between 3.5 and 6.9, which is significantly smaller than that in the 3GPP TR 38.901 model. The largest number of clusters appears in the downlink LoS case, which contradicts the common sense that the number of clusters is smaller in the LoS condition. In our opinion, the number of clusters should correlate with the number of scatterers around the transceiver, rather than the LoS or NLoS conditions. For example, even though position 7 is an LoS point, it can still have a large number of clusters because of the rich scatterers around it. We summarize the reference results of UMi scenarios in Table 5. From the table, we can see that the number of clusters is between 2.2 and 6.5 in LoS conditions, and between 2.3 and 10.33 in NLoS conditions. These values are obviously smaller than those in the 3GPP TR 38.901 standard model.

Table 5 Average cluster number in UMi scenarios

Reference	Frequency (GHz)	Cluster number	
		LoS	NLoS
Ko et al. (2017)	28	–	4.58
Nguyen et al. (2016)	15	5.67	10.33
	28	6.50	10.33
Park et al. (2016)	28	2.20	2.30
	38	5.90	6.60
Zhang PZ et al. (2020)	28	–	4.46
	39	–	3.35
	28	3.50	4.80
	39	2.60	3.82

5.2 Cluster width and cluster power in lobe-shaped clusters

Cluster width is an important parameter in lobe-shaped clusters. It reflects the angle occupation of each cluster.

After clustering the MPCs, we can determine the cluster width $W_{n,k}$ and cluster power $P_{n,k}$. The subscript $\{n, k\}$ means the n^{th} cluster at the k^{th}

measurement position. The mean width of the cluster is 18.3° in the uplink and 21.3° in the downlink. We assign all clusters to four ranges according to their widths:

- (1) $R_1 : 0^\circ \leq W_{n,k} < 10^\circ$.
- (2) $R_2 : 10^\circ \leq W_{n,k} < 30^\circ$.
- (3) $R_3 : 30^\circ \leq W_{n,k} < 60^\circ$.
- (4) $R_4 : W_{n,k} \geq 60^\circ$.

Then, the number of clusters that belong to each range is recorded. For example, the number of clusters that belong to R_1 in the uplink is represented by $N_{R_1}^{\text{UL}}$, and its percentage is derived as

$$\text{Per}_{\text{num},R_1}^{\text{UL}} = \frac{N_{R_1}^{\text{UL}}}{\sum_{i=1}^4 N_{R_i}^{\text{UL}}} \times 100\%. \quad (9)$$

The cluster number percentage in the downlink is calculated by the same method, but the superscript is changed to DL.

From Fig. 9a we can see that the cluster width is concentrated mainly in $[0^\circ, 10^\circ)$. The width of some clusters is 0 because there is only one ray in these clusters. The percentage of these clusters is 10% and 12.5% in the uplink and downlink conditions, respectively. The percentage of clusters whose width

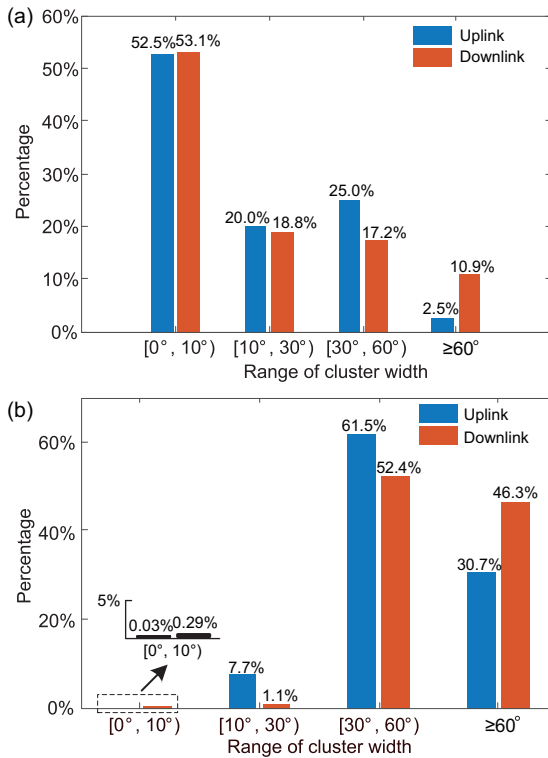


Fig. 9 Percentage of cluster width (a) and cluster power (b) in different ranges

is $\leq 30^\circ$ is similar in the uplink and downlink, but the proportion is significantly different when the cluster width is $\geq 30^\circ$. In downlink conditions, more clusters are distributed in the R_4 range. The small distance between the UT and the reflectors increases the effective reflection surface area. Correspondingly, more clusters with large widths appear in downlink conditions.

The average cluster powers of the uplink and downlink are -11.4 dB and -8.9 dB, respectively. The percentage of different power ranges is also calculated. For example, the power percentage of R_1 is derived as

$$\text{Per}_{\text{power},R_1}^{\text{UL}} = \frac{P_{R_1}^{\text{UL}}}{\sum_{i=1}^4 P_{R_i}^{\text{UL}}} \times 100\%, \quad (10)$$

where $P_{R_1}^{\text{UL}}$ is the summed power of clusters belonging to R_1 in the uplink. From Fig. 9b, we can see that although the number of clusters in R_1 is very large ($\geq 50\%$ of the total number), their occupied power proportion is very small ($\leq 0.3\%$). The clusters whose width is $\geq 30^\circ$ have $\geq 90\%$ of the total power.

To explore the relationship between cluster width $W_{n,k}$ and cluster power $P_{n,k}$, we use an exponential function to fit the curve:

$$W_{n,k} = p_1 \exp(p_2 P_{n,k}), \quad (11)$$

where p_1 and p_2 are the fitting parameters. From Fig. 10, we can see that the cluster width increases with the cluster power. In the uplink, $p_1 = 67.12$ and $p_2 = 0.0503$. The growth rate is a little higher in the downlink condition, with $p_1 = 72.08$ and $p_2 = 0.0517$.

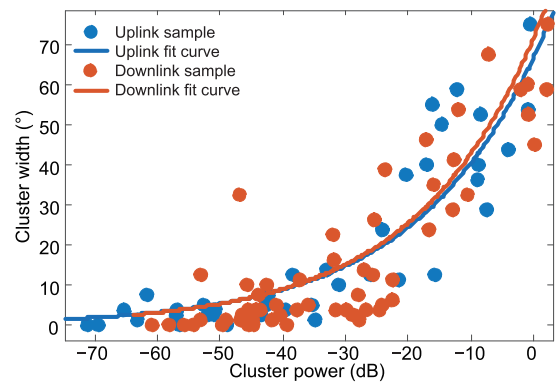


Fig. 10 Relationship between cluster power and cluster width

6 Azimuth angles of arrival of clusters and rays

6.1 Generation of cluster AoAs

Generation of the cluster angle is an important step in wireless channel simulations. It affects the small-scale features of the simulated channel. There are two approaches for determining the cluster AoA. The first uses the distribution of composite PAS of clusters. This approach is adopted by the ITU-R M.2412 (ITU-R, 2017), 3GPP TR 38.901, and WINNER II standard channel models. In this approach, the composite PAS follows a certain distribution, such as the wrapped Gaussian or Laplacian (Nie et al., 2008), and then generates the cluster angle with the foreknowledge of clutter power. The second approach generates the cluster angle using its own distribution without considering cluster power (Luo et al., 2014; Zhang JH et al., 2014). This approach is adopted by the TCSL, QuaDRiGa v2.2.0 (Jaekel et al., 2019), and mmMAGIC models. In this section, we verify these two approaches using our measurement results.

In the WINNER II and 3GPP TR 38.901 standard channel models, the AoA of the n^{th} cluster is generated as

$$\phi_n = X_n \phi'_n + Y_n + \phi_{\text{LoS}}, \quad (12)$$

where X_n is a random variable with uniform distribution to the discrete set of $\{-1, 1\}$, $Y_n \sim N(0, (\phi_{\text{ASA}}/7)^2)$, and ϕ_{LoS} is the AoA of the LoS direction. As in the explanation of the WINNER II and 3GPP TR 38.901 models, the azimuth composite PAS of all clusters is modeled as a wrapped Gaussian distribution, and ϕ'_n is determined by applying the inverse Gaussian function:

$$\phi'_n = \frac{1}{C_\phi} 2(\phi_{\text{ASA}}/1.4) \sqrt{-\ln(P_n/\max_n(P_n))}, \quad (13)$$

where P_n is the normalized power of the n^{th} cluster, ϕ_{ASA} is the root mean square (RMS) angular spread of the AoA, and C_ϕ is a scaling factor related to the cluster number and the K factor. When the unit of power is identified as dB, the composite PAS in the azimuth will change into a quadratic function as shown in Fig. 11.

Because the cluster number and the angular spread are different in the uplink and downlink, the

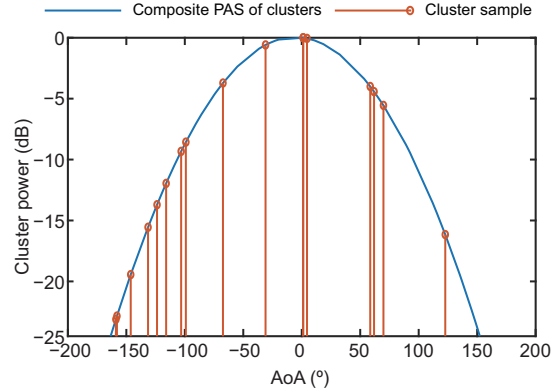


Fig. 11 An example of the composite PAS in the azimuth of all clusters

In this composite PAS (Meinilä et al., 2009), $\phi_{\text{LoS}} = 0^\circ$, the random variable Y_n is neglected, and the maximum power is set to 0 dB

composite PASs vary significantly in these two conditions. The composite PASs of different measurement positions are plotted in Fig. 12. The maximum power of the PAS is set to 0 dB, and the maximum power angle is aligned at $\phi_n = 0^\circ$ to leave out the effect of ϕ_{LoS} . From Fig. 12a we can see that many uplink clusters (positions 3, 4, 8, and 10) distribute only at one side of the ϕ_{LoS} , but according to Eq. (13), the generated angles should distribute on both sides of ϕ_{LoS} because the random variable X_n

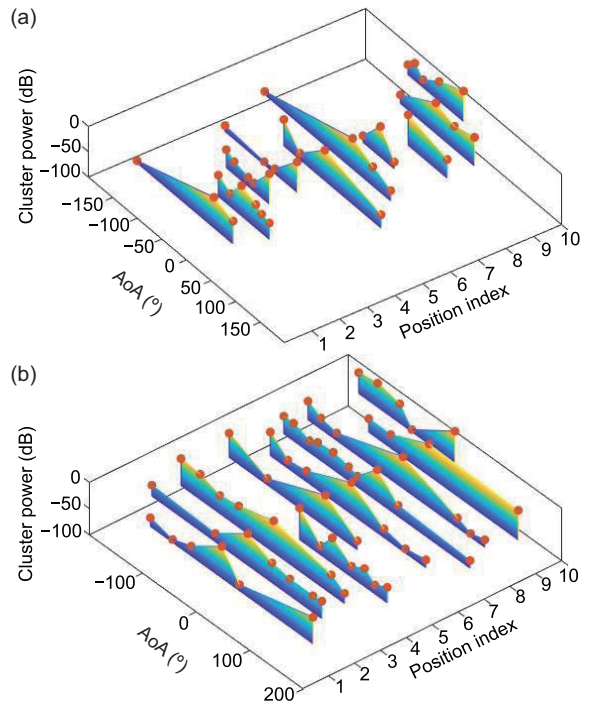


Fig. 12 Composite PASs of clusters at different measurement positions: (a) uplink; (b) downlink

uniformly distributes to the discrete set of $\{-1, 1\}$. The main reason for this is our measurement environment. There is no building on the east side of the BS to produce reflections; thus, the clusters distribute only on one side of the PASs. Although this unsymmetrical distribution rarely occurs in downlink conditions, as shown in Fig. 12b, only the PASs of positions 4 and 10 are single-side distributed in the downlink, and their PASs have a longer trail than the uplink due to the larger ϕ_{ASA} .

To verify whether our angle power spectrum is consistent with that in the standard model, we also use a quadratic function to fit PASs in Fig. 12. Surprisingly, the R^2 values in most curve-fitting results are negative, which means that our PASs are more subject to a uniform distribution than to a wrapped Gaussian distribution. Only the curve-fittings of positions 1, 7, and 8 in uplink conditions have positive R^2 values, and their range is from 0.8603 to 1. This is because positions 1, 7, and 8 have a small number of clusters (no more than 3), not because they obey a wrapped Gaussian distribution.

Using the distribution of the cluster angle to generate the AoA is another alternative method. The azimuth angles are created from a Gaussian normal distribution in the mmMAGIC model, and from a uniform distribution in the TCSL and QuaDRiGa v2.2.0 models. Here, we also use our results to test these two distributions. As shown in Fig. 13, the uplink AoA distribution is more similar to a Gaussian distribution and the downlink AoA distribution is like a uniform distribution. To determine the AoA distribution in a more precise way, we use the one-sample Kolmogorov-Smirnov (KS) test to determine the quality of the distribution fittings. The p value in the KS test is the probability of observing a test statistic as extreme as, or more extreme than, the observed value under the null hypothesis. Small values of p cast doubt on the validity of the null hypothesis. The p values of the measurement are listed in Table 6, and we can see that the Gaussian distribution is an appropriate description for the cluster AoA in uplink and downlink conditions.

Table 6 p values of the KS test in the measurement

Condition	p	
	Gaussian	Uniform
Uplink	0.2829	0.1119
Downlink	0.5519	0.3319

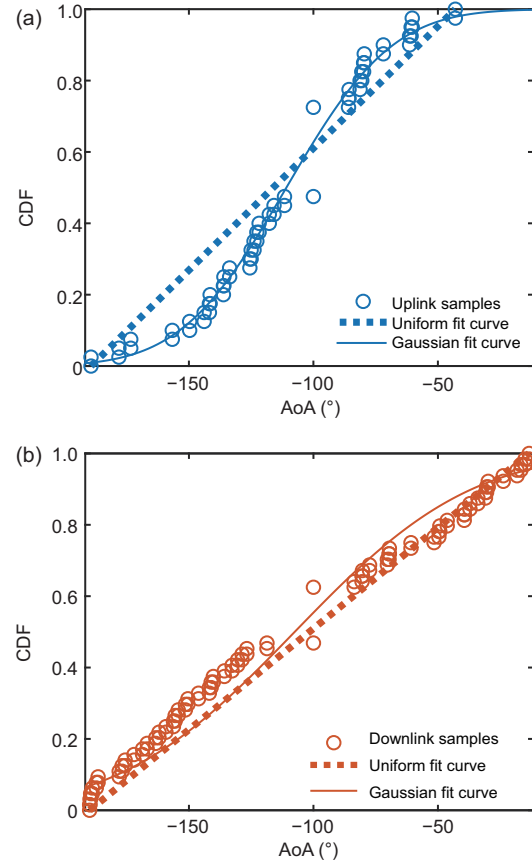


Fig. 13 Distribution of the cluster AoA in the uplink (a) and downlink (b)

6.2 A new model for ray AoA and power

There is also a modeling element that is smaller than the cluster in wireless channel models. This element is called a “ray” in the ITU-R M.2412, 3GPP TR 38.901, and WINNER II models, and a “subpath” in QuaDRiGa and mmMAGIC models. Here, we use “ray” to represent this smallest modeling element and discuss the generation of its AoA and power.

In standard models, the processes of deriving ray angles and power are considered as two independent steps. For ray angles, the ITU-R M.2412, 3GPP TR 38.901, WINNER II, and QuaDRiGa channel models use the same method. They split the cluster into M rays; the typical value of M is 20. Then, ray angles are defined as having a small angle drift around the cluster angle. For example, the AoA of the m^{th} ray in the n^{th} cluster is derived as

$$\phi_{n,m} = \phi_n + c_{ASA}\alpha_m, \quad (14)$$

where c_{ASA} is the cluster-wise ASA, and α_m is the offset factor of the m^{th} ray. c_{ASA} is decided by the

scenario type. The values of α_m for the 20 rays are restricted as in Table 7. In the mmMAGIC model, for the generation of ray AoAs, Eq. (14) can be used as well, but the offset factor has a different definition. It is calculated as

$$\alpha_m = \begin{cases} \ln\left(\frac{2m}{M}\right)/\sqrt{2}, & m < M/2, \\ -\ln\left(\frac{2(M-m)}{M}\right)/\sqrt{2}, & m \geq M/2. \end{cases} \quad (15)$$

Table 7 α_m in the ITU-R M.2412, 3GPP TR 38.901, WINNER II, and QuaDRiGa models

Ray number m	α_m	Ray number m	α_m
1, 2	± 0.0447	11, 12	± 0.6797
3, 4	± 0.1413	13, 14	± 0.8844
5, 6	± 0.2492	15, 16	± 1.1481
7, 8	± 0.3715	17, 18	± 1.5195
9, 10	± 0.5129	19, 20	± 2.1551

The number of rays is restricted to 20 for LoS and 26 for NLoS in the mmMAGIC model. In the TCSL model, the number of rays is defined to follow the discrete uniform distribution, $M \sim \text{DU}[1, 30]$. The AoA of the m^{th} ray in the n^{th} lobe is generated as

$$\phi_{n,m} = \phi_n + \Delta\phi, \quad (16)$$

where $\Delta\phi \sim N(0, c_{\text{ASA}})$.

The parameter c_{ASA} is very important in the generation of ray AoAs in different models. We calculate the mean c_{ASA} for each position and list the results in Table 3. By averaging the c_{ASA} for the uplink and downlink, we compare our results with those of the standard models in Table 4. A smaller c_{ASA} is observed in the TCSL model and our measurement. We both cluster the MPCs in a lobe shape, but our measured c_{ASA} is smaller, and is only one-third of that of the TCSL model. The MPC extraction process sharpens the lobes. Another interesting finding is that the link condition does not have a high impact on the c_{ASA} in the TCSL model and our measurement. The c_{ASA} just varies from 8.5° to 10.1° in the TCSL model, and varies from 2.7° to 4.1° in our measurement, but in the 3GPP TR 38.901 and mmMAGIC models, the c_{ASA} changes from 3° to 22° . This is because the 3GPP TR 38.901 and mmMAGIC models consider the power, delay, and angle simultaneously when clustering the MPCs. These characteristics are all affected by the link condition.

However, in the lobe-shaped cluster method, we consider only the power and the angle, which weakens the effect of link conditions.

The ITU-R M.2412, 3GPP TR 38.901, and WINNER II channel models uniformly distribute the power of clusters to each ray:

$$P_{n,m} = \frac{P_n}{M}. \quad (17)$$

In the mmMAGIC model, the ray power is determined by the exponential function:

$$P'_{n,m} = \exp\left(-\Delta\tau_{n,m} \frac{r_\mu - 1}{r_\mu c_{\text{DS}}}\right), \quad (18)$$

where $\Delta\tau_{n,m}$ is the relative delay of the ray, r_μ is the delay distribution proportionality factor, and c_{DS} is the intra-cluster delay spread. Then $P'_{n,m}$ is normalized to ensure that the summed cluster power equals P_n :

$$P_{n,m} = P_n \frac{P'_{n,m}}{\sum_{m=1}^M P'_{n,m}}. \quad (19)$$

The power generation of rays in the TCSL model is similar to that in the mmMAGIC model, but Eq. (18) needs to be rewritten as

$$P'_{n,m} = \overline{P_{n,0}} \exp\left(-\frac{\Delta\tau_{n,m}}{\gamma}\right) 10^{\frac{U_{n,m}}{10}}, \quad (20)$$

where $\overline{P_{n,0}}$ is the average power of the first received rays, γ is the delay constant, and $U_{n,m}$ is a lognormal random variable following $U_{n,m} \sim N(0, \sigma_U)$.

In this part, we try to find the relationship between the ray AoA and power. The ray AoA and power are plotted together in Fig. 14. In each cluster, the largest ray power is normalized to 0 dB,

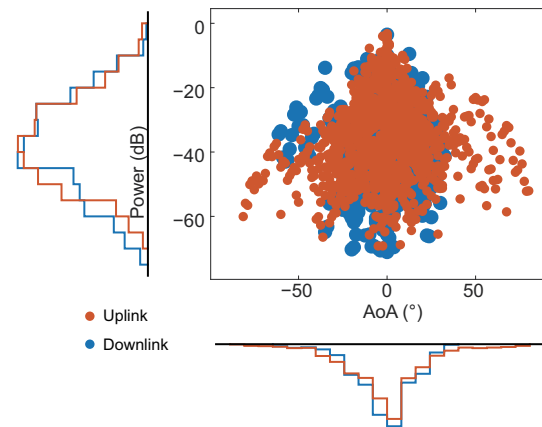


Fig. 14 Distribution of ray AoAs and power

and its corresponding AoA is aligned to 0° . From Fig. 14, we can see that the ray power in the uplink and downlink are similar to a normal distribution, which is different from the definition in standard models. In addition, we see a correlation between the ray AoA and power. To verify this correlation and find a more suitable method of generating ray AoA and power, we propose a multivariate Gaussian distribution model. Its joint probability density is as follows:

$$p(x_1, x_2) = \frac{1}{2\pi|\Sigma|^{\frac{1}{2}}} \exp\left\{-\frac{1}{2}[(x-\mu)^T \Sigma^{-1}(x-\mu)]\right\}, \quad (21)$$

where $x = [\phi_{n,m}, P_{n,m}]$, μ is the mean vector of x , and Σ is the covariance matrix. After fitting our results in Fig. 15, $\mu = [-2.5, -38.2]$ and $\Sigma = \begin{bmatrix} 254.4 & -2.6 \\ -2.6 & 193.2 \end{bmatrix}$ in the uplink. The covariance of ray AoA and power is -2.6 , which is smaller than 1% of ray AoA/power self-variance. Thus, it is reasonable to believe that ray AoA and power are distributed independently in the uplink, while in the

downlink, $\mu = [-1.1, 36.8]$ and $\Sigma = \begin{bmatrix} 546.1 & 23.9 \\ 23.9 & 157.6 \end{bmatrix}$.

The covariance of ray AoA and power increases to 23.9, which verifies the correlation between the ray AoA and power.

In the proposed model, we establish a two-dimensional Gaussian distribution for the ray power and angle, which is more random in angle distribution, and verifies the correlation between the ray power and angle. Another advantage of this model is that it does not need the delay distribution to decide the ray power. The proposed model can simultaneously generate the ray power and angle.

7 Conclusions

This study has presented spatial characteristics in the uplink and downlink through a measurement conducted in a UMi scenario at 28 GHz. To improve the MPC resolution, we use the SAGE algorithm to extract multipath information and delete the effect of rotatable horn antennas. By matching the PASs of the AoA in the uplink and downlink, we find that the first-order reflection and direct paths reign in all propagation types. Moreover, because there are more scatterers near the UT end, the directions of the arrival wave are more diffuse, and the superposition of MPCs is more severe in the downlink. To construct the connection between the TCSL model and the 3GPP 38.901 model, we cluster the MPCs in a lobe shape. Compared with the 3GPP TR 38.901 and mmMAGIC models, the TCSL model and our measurement have a smaller number of clusters and smaller intra-cluster ASA. Furthermore, the link conditions (uplink or downlink, LoS or NLoS) have little effect on angular characteristics because the lobe-shaped cluster method considers only the PAS. The power in the lobes is continuous, and there are few intervals in the clustered lobes. Finally, we study the generation of clusters and ray AoAs. We find that the measured PAS of the AoA does not always obey the wrapped Gaussian distribution in the 3GPP TR 38.901 model. Generating the AoA of clusters as a Gaussian distribution is a recommended method. In addition, we propose to use a multivariate Gaussian distribution to generate ray power and AoA, which can reflect the correlation between the ray AoA and power.

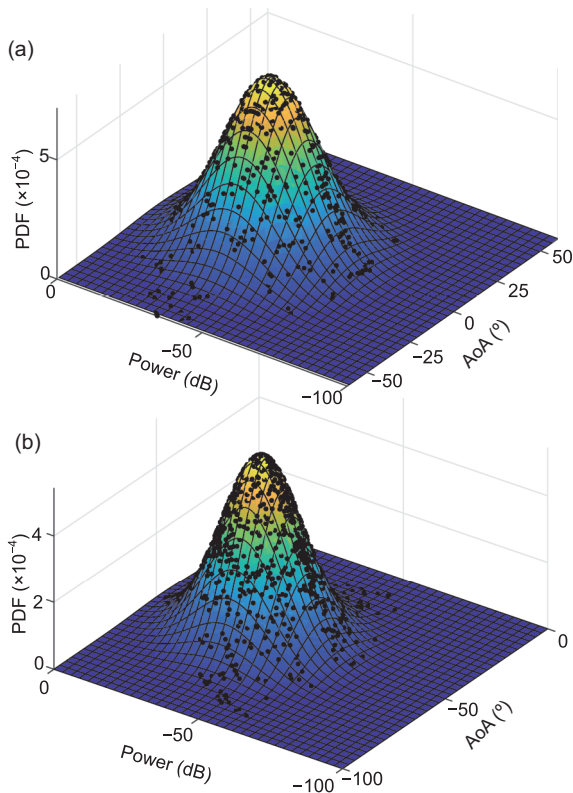


Fig. 15 Joint probability density function (PDF) of ray AoAs and power in the uplink (a) and downlink (b)

Contributors

Tao JIANG and Pan TANG designed the research. Tao JIANG processed the data. Tao JIANG and Jianhua ZHANG drafted the manuscript. Jianhua ZHANG and Lei TIAN helped organize the manuscript. Tao JIANG, Jianhua ZHANG, Pan TANG, and Lei TIAN revised and finalized the paper.

Compliance with ethics guidelines

Tao JIANG, Jianhua ZHANG, Pan TANG, and Lei TIAN declare that they have no conflict of interest.

References

- 3GPP, 2019. Study on Channel Model for Frequencies from 0.5 to 100 GHz. Technical Report, TR 38.901.
- Alatossava M, Hentila L, Holappa VM, et al., 2007. Comparison of outdoor to indoor and indoor to outdoor MIMO propagation characteristics at 5.25 GHz. *IEEE 65th Vehicular Technology Conf*, p.445-449. <https://doi.org/10.1109/VETECS.2007.103>
- Bigler L, Lin HP, Jeng SS, et al., 1995. Experimental direction of arrival and spatial signature measurements at 900 MHz for smart antenna systems. *IEEE 45th Vehicular Technology Conf*, p.55-58. <https://doi.org/10.1109/VETEC.1995.504828>
- Fleury BH, Tschudin M, Heddergott R, et al., 1999. Channel parameter estimation in mobile radio environments using the SAGE algorithm. *IEEE J Sel Areas Commun*, 17(3):434-450. <https://doi.org/10.1109/49.753729>
- Foo SE, Beach MA, Karlsson P, et al., 2002. Spatio-temporal investigation of UTRA FDD channels. *3rd Int Conf on 3G Mobile Communication Technologies*, p.175-179. <https://doi.org/10.1049/cp:20020384>
- Gao XX, Tian L, Tang P, et al., 2016. Channel characteristics analysis of angle and clustering in indoor office environment at 28 GHz. *IEEE 84th Vehicular Technology Conf*, p.1-5. <https://doi.org/10.1109/VTCFall.2016.7880929>
- Hamida STB, Pierrot JB, Castelluccia C, 2010. Empirical analysis of UWB channel characteristics for secret key generation in indoor environments. *21st Annual IEEE Int Symp on Personal, Indoor and Mobile Radio Communications*, p.1984-1989. <https://doi.org/10.1109/PIMRC.2010.5671596>
- He S, Dong X, Tian Z, et al., 2009. On the empirical evaluation of spatial and temporal characteristics of ultra-wideband channel. *IEEE 69th Vehicular Technology Conf*, p.1-5. <https://doi.org/10.1109/VETECS.2009.5073730>
- ITU-R, 2017. Guidelines for Evaluation of Radio Interface Technologies for IMT-2020. Technical Report, M.2412-0.
- Jaeckel S, Raschkowski L, Börner K, et al., 2019. Quasi Deterministic Radio Channel Generator User Manual and Documentation. Technical Report, v2.2.0.
- Jiang T, Tian L, Tang P, et al., 2017. Basestation 3-dimensional spatial propagation characteristics in urban microcell at 28 GHz. *11th European Conf on Antennas and Propagation*, p.3167-3171. <https://doi.org/10.23919/EuCAP.2017.7928845>
- Jiang T, Zhang JH, Shafi M, et al., 2020. The comparative study of S-V model between 3.5 and 28 GHz in indoor and outdoor scenarios. *IEEE Trans Veh Technol*, 69(3):2351-2364. <https://doi.org/10.1109/TVT.2019.2963076>
- Ko J, Cho YJ, Hur S, et al., 2017. Millimeter-wave channel measurements and analysis for statistical spatial channel model in in-building and urban environments at 28 GHz. *IEEE Trans Wirel Commun*, 16(9):5853-5868. <https://doi.org/10.1109/TWC.2017.2716924>
- Luo QL, Pei F, Zhang JH, et al., 2014. 3D MIMO channel model based on field measurement campaign for UMA scenario. *IEEE Wireless Communications and Networking Conf*, p.171-176. <https://doi.org/10.1109/WCNC.2014.6951942>
- Lv YJ, Yin XF, Zhang C, et al., 2019. Measurement-based characterization of 39 GHz millimeter-wave dual-polarized channel under foliage loss impact. *IEEE Access*, 7:151558-151568. <https://doi.org/10.1109/ACCESS.2019.2945042>
- Meinilä J, Kyösti P, Jämsä T, et al., 2009. WINNER II channel models. In: Döttling M, Mohr W, Osseiran A (Eds.), *Radio Technologies and Concepts for IMT-Advanced*. Wiley, Chichester, UK, p.39-92.
- Nguyen SLH, Haneda K, Putkonen J, 2016. Dual-band multipath cluster analysis of small-cell backhaul channels in an urban street environment. *IEEE Globecom Workshops*, p.1-6. <https://doi.org/10.1109/GLOCOMW.2016.7848881>
- Nie X, Zhang JH, Zhang Y, et al., 2008. An experimental investigation of wideband MIMO channel based on indoor hotspot NLOS measurements at 2.35 GHz. *IEEE Global Telecommunications Conf*, p.1-5. <https://doi.org/10.1109/GLOCOM.2008.ECP.760>
- Park JJ, Liang JY, Lee J, et al., 2016. Millimeter-wave channel model parameters for urban microcellular environment based on 28 and 38 GHz measurements. *IEEE 27th Annual Int Symp on Personal, Indoor, and Mobile Radio Communications*, p.1-5. <https://doi.org/10.1109/PIMRC.2016.7794731>
- Pedersen KI, Mogensen PE, Frederiksen F, 1999. Joint directional properties of uplink and downlink channel in mobile communications. *Electron Lett*, 35(16):1311-1312. <https://doi.org/10.1049/el:19990889>
- Peter M, Haneda K, Nguyen SLH, et al., 2017. Measurement Results and Final mmMAGIC Channel Models. Technical Report, H2020-ICT-671650-mmMAGIC/D2.2.
- Rappaport TS, Gutierrez F, Ben-Dor E, et al., 2013. Broadband millimeter-wave propagation measurements and models using adaptive-beam antennas for outdoor urban cellular communications. *IEEE Trans Antenn Propag*, 61(4):1850-1859. <https://doi.org/10.1109/TAP.2012.2235056>
- Samimi MK, Rappaport TS, 2016a. 3-D millimeter-wave statistical channel model for 5G wireless system design. *IEEE Trans Microw Theory Techn*, 64(7):2207-2225. <https://doi.org/10.1109/TMTT.2016.2574851>
- Samimi MK, Rappaport TS, 2016b. Local multipath model parameters for generating 5G millimeter-wave 3GPP-like channel impulse response. *10th European Conf on Antennas and Propagation*, p.1-5. <https://doi.org/10.1109/EuCAP.2016.7481410>

- Shafi M, Zhang JH, Tataria H, et al., 2018. Microwave vs. millimeter-wave propagation channels: key differences and impact on 5G cellular systems. *IEEE Commun Mag*, 56(12):14-20.
<https://doi.org/10.1109/MCOM.2018.1800255>
- Tang P, Zhang JH, Shafi M, et al., 2018. Millimeter wave channel measurements and modelling in an indoor hotspot scenario at 28 GHz. *IEEE 88th Vehicular Technology Conf*, p.1-5.
<https://doi.org/10.1109/VTCFall.2018.8690888>
- You XH, Wang CX, Huang J, et al., 2020. Towards 6G wireless communication networks: vision, enabling technologies, and new paradigm shifts. *Sci China Inform Sci*, 64:110301.
<https://doi.org/10.1007/s11432-020-2955-6>
- Zhan JN, Zhang JH, Tian L, et al., 2018. Comparative channel study of ray tracing and measurement for an indoor scenario at 28 GHz. *12th European Conf on Antennas and Propagation*, p.1-5.
<https://doi.org/10.1049/cp.2018.1044>
- Zhang JH, Pan C, Pei F, et al., 2014. Three-dimensional fading channel models: a survey of elevation angle research. *IEEE Commun Mag*, 52(6):218-226.
<https://doi.org/10.1109/MCOM.2014.6829967>
- Zhang JH, Tang P, Tian L, et al., 2017. 6-100 GHz research progress and challenges from a channel perspective for fifth generation (5G) and future wireless communication. *Sci China Inform Sci*, 60(8):080301.
<https://doi.org/10.1007/s11432-016-9144-x>
- Zhang JH, Tang P, Yu L, et al., 2020. Channel measurements and models for 6G: current status and future outlook. *Front Inform Technol Electron Eng*, 21(1):39-61.
<https://doi.org/10.1631/FITEE.1900450>
- Zhang PZ, Li J, Wang HB, et al., 2018. Indoor small-scale spatiotemporal propagation characteristics at multiple millimeter-wave bands. *IEEE Antenn Wirel Propag Lett*, 17(12):2250-2254.
<https://doi.org/10.1109/LAWP.2018.2872051>
- Zhang PZ, Yang BS, Yi C, et al., 2020. Measurement-based 5G millimeter-wave propagation characterization in vegetated suburban macrocell environments. *IEEE Trans Antenn Propag*, 68(7):5556-5567.
<https://doi.org/10.1109/TAP.2020.2975365>
- Zhao XW, Du F, Geng SY, et al., 2019. Neural network and GBSM based time-varying and stochastic channel modeling for 5G millimeter wave communications. *China Commun*, 16(6):80-90.
<https://doi.org/10.23919/JCC.2019.06.007>